Activity and Durability of Platinum-Based Electrocatalysts Supported on Bare or Fluorinated Nanostructured Carbon Substrates

Tristan Asset, Raphaël Chattot, Frédéric Maillard, Laetitia Dubau, Yasser Ahmad, Nicolas Batisse, Marc Dubois, Katia Guérin, Fabien Labbé, Rudolf Metkemeijer, et al.

▶ **To cite this version:**

Tristan Asset, Raphaël Chattot, Frédéric Maillard, Laetitia Dubau, Yasser Ahmad, et al.. Activity and Durability of Platinum-Based Electrocatalysts Supported on Bare or Fluorinated Nanostructured Carbon Substrates. Journal of The Electrochemical Society, 2018, 165 (6), pp.F3346-F3358. 10.1149/2.031806jes] . hal-01785111

HAL Id: hal-01785111

https://minesparis-psl.hal.science/hal-01785111v1

Submitted on 4 May 2018

HAL is a multi-disciplinary open access archive for the deposit and dissemination of scientific research documents, whether they are published or not. The documents may come from teaching and research institutions in France or abroad, or from public or private research centers.

L'archive ouverte pluridisciplinaire **HAL**, est destinée au dépôt et à la diffusion de documents scientifiques de niveau recherche, publiés ou non, émanant des établissements d'enseignement et de recherche français ou étrangers, des laboratoires publics ou privés.

JES Focus Issue on Proton Exchange Membrane Fuel Cell (PEMFC) Durability

Activity and Durability of Platinum-Based Electrocatalysts Supported on Bare or Fluorinated Nanostructured Carbon Substrates

Tristan Asset,[1] Raphaël Chattot,[1] Frédéric Maillard,[1,*] Laetitia Dubau,[1,*] Yasser Ahmad,[2,3] Nicolas Batisse,[2] Marc Dubois,[2] Katia Guérin,[2] Fabien Labbé,[4] Rudolf Metkemeijer,[4] Sandrine Berthon-Fabry,[4] and Marian Chatenet[1,4,5,*,z]

[1] *Université Grenoble Alpes, CNRS, Grenoble-INP (Institute of Engineering, Université Grenoble Alpes), Université Savoie-Mont-Blanc, LEPMI, 38000 Grenoble, France*
[2] *Clermont Université, CNRS, ICCF, F-63000 Clermont-Ferrand, France*
[3] *College of Engineering, Mechanical Engineering Department, Fahad Bin Sultan University, Tabuk, Saudi Arabia*
[4] *MINES ParisTech, PSL Research University PERSEE, F-06904 Sophia Antipolis Cedex, France*
[5] *French University Institute, Paris, France*

Nanostructured carbons were fluorinated and used as supports for Pt nanoparticles deposition using a modified polyol route. The resulting materials exhibited similar Pt nanoparticles sizes, but different agglomeration rates. The electrocatalysts were tested toward the oxygen reduction reaction, and their stability was investigated in simulated load cycling ($0.6 < E < 1.0$ V vs. RHE) or start-up/shutdown ($1.0 < E < 1.5$ V vs. RHE) protocols. Irrespective the support material, the former protocol caused Pt nanocrystallites dissolution/redeposition via Ostwald ripening, mildly decreasing the electrochemically-active surface area and ORR activity. In contrast, the carbon supports were strongly corroded after the start-up/shutdown protocol, resulting in pronounced detachment/agglomeration of Pt nanocrystallites, albeit in absence of significant particle-size growth. Fluorination had different effects on the stability of structurally-ordered and structurally-disordered carbons: beneficial effects were observed for the latter whereas the former was affected negatively. "Free" dangling groups present in structurally-disordered carbon, known to be prone to preferential oxidation in PEMFC environment, combine with the fluorine precursors upon fluorination, leading to formation of more robust C-F bonds versus oxidation than original C-O bonds. In contrast, fluorination of structurally-ordered carbon creates structural disorder (C-C bonds are broken), leading to promotion of electrochemical corrosion.
© The Author(s) 2018. Published by ECS. This is an open access article distributed under the terms of the Creative Commons Attribution 4.0 License (CC BY, http://creativecommons.org/licenses/by/4.0/), which permits unrestricted reuse of the work in any medium, provided the original work is properly cited. [DOI: 10.1149/2.031806jes]

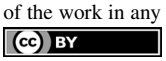

Manuscript submitted December 21, 2017; revised manuscript received April 19, 2018. Published May 2, 2018. *This paper is part of the JES Focus Issue on Proton Exchange Membrane Fuel Cell (PEMFC) Durability.*

The implementation of nanostructured carbon-supported platinum electrocatalysts in proton exchange membrane fuel cell (PEMFC) electrodes since the 1990s[1–4] enabled utilization factor (u_{Pt}) approaching 100%; this technological breakthrough is at the origin of the high electrical performances that are delivered by current systems.[5–8] Since then, the performances of PEMFCs have continuously improved, notably in terms of (i) reduction of Pt-group metal (PGM) loading, and of (ii) increase of the power density, durability and reliability on the field, which has enabled their recent release on the market for portable, automotive and stationary applications. Despite successes of the PEMFC technology, durability and reliability of the core materials, and electrodes should be further improved. In this regard, it is well-established that the carbon substrate of the Pt-based nanoparticles is corroded in the harsh operating conditions of a PEMFC cathode.[9–14] Carbon corrosion has a thermodynamical origin (carbon oxidizes into CO_2 at $E > 0.207$ V vs. the reversible hydrogen electrode, RHE),[15] which renders the process inevitable at the cathode. Besides, the intimate contact of the carbon with Pt nanoparticles weakens electrochemical resistance to corrosion, as Pt catalyzes this reaction.[9,16–20] Numerous parameters are known to aggravate the process, such as incursions to high electrode potential values e.g. during start/stop or fuel starvation events,[21–28] the nature of the gas atmosphere or the relative humidity[29–32] and even the properties of the anode catalyst layer.[33] Carbon corrosion alters the physico-chemical properties of the cathode catalyst layer, both by (i) altering the dispersion of the Pt nanoparticles (which decreases the electrochemically active surface area, ECSA),[10,34] by (ii) increasing the hydrophilicity of the catalyst layer and by (iii) destroying its porous texture. All three processes yield oxygen mass-transport hindrances and severely degrade the practical performances of the PEMFC cathode and therefore of the entire system.[8] Different material strategies have been proposed to strengthen the robustness of conductive supports for Pt-based nanoparticles in PEMFC cathodes.

One of the most efficient ways is to use graphitized carbon supports, as such structurally-ordered carbon supports are more resistant to CO_2 formation upon corrosion.[35–42] This higher resistance to corrosion does however not grant durability in operation: Castanheira et al.[12,39] and Linse et al.[19] demonstrated that in presence of Pt nanoparticles in contact with the carbon support, the tougher behavior of graphitic carbon is only a reality above 1.0 V vs. RHE; below this value, carbon corrosion is assisted by the catalytic role of Pt, and hardly any difference in the rate of corrosion is witnessed between nanostructured carbons of various levels of graphitization/organization. To be more specific, below 1.0 V vs. RHE, the various carbon surface groups that spontaneously form above $E = 0.2$ V vs. RHE have the propensity to back spill-over to the surface of platinum nanoparticles (which is, at least to some extent, free of oxides and therefore available to welcome CO_{ad}-like adsorbates),[18] where they can be electrooxidized into CO_2 according to the well-known Langmuir-Hinshelwood mechanism (in essence, this pathway resembles that occurring during a CO_{ads} stripping experiment).[43] Of course, this pathway is even faster in conditions of base-load potential cycling, i.e. when the electrode potential is scanned back and forth above/below the onset of Pt-oxides formation.[12,44] As a result, the strategy of using a more graphitized carbon surface is only efficient to mitigate the carbon corrosion experienced at idling or in start/stop and fuel starvation conditions in a real PEMFC;[37,39] although this is already a real achievement and enabled to prolong the durability of stationary PEMFCs on the field from a few 100 hours[10,34] to several 1,000 hours[12–14,25] (from the former to the latter studies, the carbon was changed from poorly graphitized to highly graphitized, resulting in much lower degradation of the cathode structure, even if the authors admit that the other components of

*Electrochemical Society Member.
[z]E-mail: Marian.Chatenet@phelma.grenoble-inp.fr

Downloaded on 2018-05-04 to IP 77.158.181.1 address. Redistribution subject to ECS terms of use (see ecsdl.org/site/terms_use) unless CC License in place (see abstract).

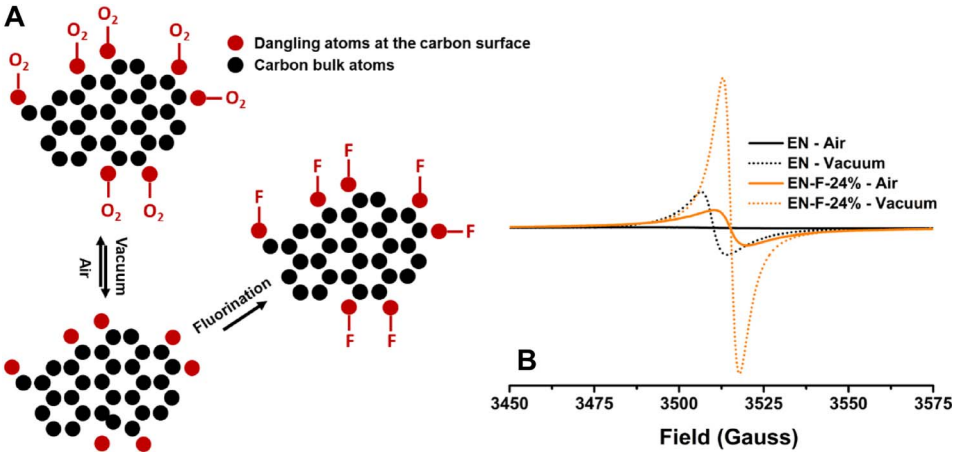

Figure 1. (A) Schematic representation of the EPR procedure used to determine the surface dangling groups of carbon and of the fluorination process: the surface dangling groups of carbon are firstly combining with fluorine atoms yielding C-F bonds. If the fluorination is further conducted, the bulk dangling groups of carbon start being fluorinated. (B) example of EPR spectra monitored for the EN sample revealing the very different density of spin in air versus in vacuum for both the EN and EN-F-24% sample.

the PEMFC were also improved in the meantime, e.g. the membrane, the electrocatalyst nanoparticles, etc.), it is not enough to warranty sufficient PEMFC durability for several 1,000 hours in automotive applications or for several 10,000 hours in stationary applications.[45,46]

For these reasons, substitutes to carbon have been studied. In particular, (semi-)conductive substrates from the metal oxides families (MO_x, with M = Ti, Sn, W, etc.) were proposed as means to limit (if not prevent) the degradation processes of the Pt-based nanoparticles support.[47–63] However, while interesting electrocatalytic performances and durability were reached in "half-cell" (usually liquid electrolyte) condition for Pt/MO_x electrocatalysts, these have not yet been translated to efficient and durable PEMFC cathodes. As a matter of fact, these substrates are very difficult to tailor in terms of specific surface area and porous texture, altering the dispersion of Pt at their surface,[59–61] and they proved less stable than one would have hoped, as they are also subjected to durability issues.[60] Non electron-conducting supports have also been proposed, e.g. the Pt/NSTF from 3M,[64–66] but these materials failed to be implemented with success in PEMFC systems on the field, owing to the difficulty to deliver stable electrocatalytic performances in non-perfectly-controlled operation.

This brief literature overview demonstrates that no practical solution is presently capable to yield stable Pt-based electrocatalysts for long-term operation in a PEMFC cathode. Besides, owing to the low-cost, high-availability, easy-shaping properties and high conductivity of nanostructured carbons, it seems wise to modify these supports to render them more resistant toward (electro)chemical oxidation. Surface modification of nanostructured carbons through grafting of thiophenol groups or diazonium salts was investigated as a potential method to improve the stability of Pt nanoparticles,[67,68] but the effect on the inherent resistance of the carbon support to corrosion was not documented in these papers. Protective coatings by conductive polymers has also been proposed,[69] but the practical electronic conductivity of polymer-coated carbon supports was shown to degrade after the deposition of the Pt nanoparticles, because the Pt^{z+} precursor may attack the polymer coating, thus yielding loss of electronic percolation and poor electrical performances.[70] Among the strategies to protect the carbon surface, fluorination soon arose as a relevant technique, owing to the inherent resistance of C-F bonds to electrooxidation.[71] This strategy has been, to some extent, explored for the protection of the carbon used in Li battery electrodes.[72,73] Fluorine-doped carbons exhibit enhanced oxygen reduction activity over their bare counterparts, both in acidic[74,75] and alkaline electrolytes.[76] Recently, fluorination of carbon supports has also been proposed to prepare Pt-based electrocatalysts for oxygen reduction in PEMFC.[77] However, it has been shown that fluorination must be conducted prior to Pt deposition at the carbon substrate, as post-fluorination of a Pt/C electrocatalyst leads to deactivation of the Pt nanoparticles. Fluorination of the carbon support enables to bind fluorine atoms to their dangling groups, the latter likely being the ones that are oxidized first during PEMFC operation.[12,78] Keeping this idea in mind, it is not surprising that steam etching of high surface area carbon blacks (i.e. preferentially corrosion of the structurally-disordered domains) enhances their resistance to corrosion in simulated PEMFC operating conditions.[79] Quantifying dangling groups of porous carbons can be achieved by Electron Paramagnetic Resonance (EPR). This technique is based on the paramagnetic properties of molecular oxygen (O_2) molecules, and on the fact that these can bind with surface dangling groups of carbon; as such, their presence or absence will affect the EPR signal of porous carbons.[80,81] Indeed, the dangling groups that exist at the surface of all porous carbons are magnetically coupled with O_2 molecules, thereby decreasing their density of spin. A simple procedure that consists of comparing the EPR spectra of a given carbon support in vacuum (in absence of O_2 molecules) and in air (in presence of O_2 molecules, enabling their coupling with dangling groups of carbon) enables to track the surface dangling groups of carbon materials, as only these ones are susceptible to interact with O_2 molecules under air (Figure 1). Hence, if one can efficiently bind these surface dangling groups of carbon with F atoms, the resulting fluorinated carbon substrate could be less prone to corrosion in PEMFC-mimicking environment than its non-fluorinated analogue.

To test this hypothesis, in the present contribution, a wide set of carbon supports featuring different structural and textural properties were used both bare and functionalized by partial fluorination. Pt nanoparticles of similar individual crystallite sizes were then deposited using a modified polyol method,[82] so that the comparison of their electrochemical activities and durabilities is not biased by any Pt nanoparticle size effect.[83–88] These in-house electrocatalysts were fully characterized by complementary physicochemical and electrochemical techniques, and then tested for the oxygen reduction reaction (ORR) in rotating disk electrode configuration, both before and after accelerated stress test (AST) procedures. These comparisons enabled to draw conclusions about the potential benefit of fluorination on the durability of Pt/C electrocatalysts.

Experimental

Carbon substrates.—The carbon substrates used in the present study are based on two sets of materials. Firstly, a commercial high surface area carbon (Imerys Graphite & Carbon, ENSACO 350 G Conductive Carbon Black, hereafter denoted by "EN") and a commercial graphitized acetylene black (YS, from SN2A: Société du Noir d'Acétylène de l'Aubette, hereafter denoted by "YS") were used for fluorination and/or Pt nanoparticles deposition without further treatment. Secondly, a carbon aerogel was prepared in-house using the well-known Pekala method.[89] The synthesis protocol has been thoroughly described in earlier contributions of the authors.[77,90] Briefly, the two precursors, resorcinol (R, 99% $C_6H_6O_2$, Alfa Aesar) and formaldehyde (F, 37 wt% CH_2O in aqueous solution stabilized with 10–15 wt% methanol) were mixed with the sodium carbonate (C,

Downloaded on 2018-05-04 to IP 77.158.181.1 address. Redistribution subject to ECS terms of use (see ecsdl.org/site/terms_use) unless CC License in place (see abstract).

99.9999% Na_2CO_3, Sigma Aldrich) catalyst in deionized water with molar ratios F/R = 2, R/C = 200 and 5 wt% solid in solution. The resulting solution was then heated at T = 358 K under confined atmosphere for one week for gelation and mechanical handling. After exchange of the water by acetone, the gel was dried in supercritical CO_2 conditions (80 bars, 310 K). The resulting organic aerogel was then pyrolyzed at T = 1323 K under nitrogen flow, leading to the carbon aerogel sample (hereafter noted "CA"). The synthesis parameters have been chosen in order to obtain carbon aerogel material with a porous 3-dimensional architecture compatible with limited diffusive overpotential in PEMFC.[91]

Fluorination of the carbon supports.—The fluorination was performed by gas-solid reaction with a defined amount of pure F_2 gas (1 L per 200 mg of carbon sample) into a nickel reactor covered with a NiF_2 passivation layer. Firstly, O_2 and moisture from air were purged thanks to a continuous flux of N_2 for t = 1 h. Then, the reactor was filled with the desired amount of fluorine and closed to favor the reaction with carbon during a set time at a dedicated fluorination temperature, that was adapted to the nature of the carbon sample. Finally, the reactive atmosphere was eliminated under N_2 flow for t = 1 h. In the case of the EN sample, fluorination was performed at room temperature during 15 min. The fluorination rate was determined by weight uptake and the atomic fluorine/carbon ratio (F/C) and was determined to be 0.24 for EN. The sample is noted EN-F-24%. The same fluorination conditions were applied to CA, giving a F/C ratio of 0.25 (sample noted CA-F-25%). For YS, different fluorination temperatures were applied for 1 h. For a fluorination temperature of T = 423 K, T = 623 K and T = 643 K, a F/C ratio of 0.05, 0.14 and 0.37 was obtained, respectively. The corresponding samples are noted: YS-F-05%, YS-F-14% and YS-F-37%, respectively.

Deposition of colloidal pt nanoparticles according to a modified polyol process.—The deposition of the Pt nanoparticles onto the various carbon supports was performed as follows: a given amount of Pt salt (H_2PtCl_6-xH_2O, 99.9% metal basis, Alfa Aesar) was first dissolved in a 2:1 ethylene glycol (Rotipuran >99.9%, Roth):deionized water (18.2 MΩ) solution (typically 88 mg of Pt salt in 100 mL of solution). Then, the solution was rendered alkaline up to pH = 12.5 and vigorously stirred under argon atmosphere during t = 1 h, prior to the temperature increase at T = 393 K, this temperature being maintained during t = 3 h. Meanwhile, the carbon support was dispersed in a 1:1 ethylene glycol:deionized water solution, aiming a theoretical loading of Pt onto the carbon support of 40 wt%. The solution containing the Pt colloidal solution and the dispersed carbon support were then mixed and the pH of the solution was decreased down to pH = 2.5 to allow the nanoparticles deposition onto the carbon support (see[82] and[92]). After t = 22 h, the solution was filtered, washed and dried for t = 45 min at T = 383 K.

Electrochemical experiments.—The electrochemical characterizations were performed in an in-house four-electrode electrochemical cell. A glassy-carbon rotating disk electrode (RDE) tip was used as working electrode. A glassy-carbon electrode was used as counter-electrode (CE) to avoid any contamination of the electrolyte by metal cations of the CE. The reference electrode was a commercial reversible hydrogen electrode (RHE, Pt/Pd-Hydrogen electrode with internal hydrogen source, HydroFlex – Gaskatel) for operation in the durability cell (operating at T = 353 K, see below), and a freshly-prepared in-house RHE for the electrochemical activity experiments, performed in a similar cell maintained at T = 298 K (see below). Finally, a Pt wire connected to the reference electrode through a capacitive bridge was used as filter to avoid the electrical noise in the electrochemical measurements.[93] The working electrode was a thin-film rotating disk electrode prepared as follows. A 0.392 $g_{Pt/C}$ L^{-1} of Pt/C suspension, composed of 5 wt% Nafion solution, corresponding to a 0.3 Nafion/Carbon ratio, (Aldrich), ultrapure water (3.6 mL) and isopropanol (1.446 mL, Roth >99.5%), was ultrasonically treated for 15 min to obtain a well-dispersed ink. One calibrated drop (10 µL) of this ink was deposited on the in-house-designed glassy-carbon RDE tip for the electrochemical tests. The resulting Pt loadings was 20 μg_{Pt} cm^{-2}. Before any experiment, the glassware was soaked with concentrated Caro's acid (96% H_2SO_4 – 30% H_2O_2 mixture) at least overnight, thoroughly rinsed with ultrapure water, and then further boiled in ultrapure water to remove any trace of sulfate anions (that could strongly adsorb at Pt sites and alter the electrochemical measurements).

Concentrated $HClO_4$ (Suprapur, Merck) was used as received to prepare the 0.1 M $HClO_4$ electrolyte solutions upon appropriate dilution in ultrapure water (18.2 MΩ cm, 1–3 ppb total organic carbon, TOC, Millipore). The electrolyte was purged with argon (Ar >99.99% Messer), carbon monoxide (CO >99.997% Messer) or oxygen (O >99.995% Messer) depending on the characterization carried-out. The accelerated stress tests were either a base load cycle procedure (succession of 15,000 cyclic voltammetries between E = 0.6 V vs. RHE and E = 1.0 V vs. RHE at a scan rate v = 50 mV s^{-1}) or a start-stop procedure (succession of 1,000 three-second potential steps between E = 1.0 V vs. RHE and E = 1.5 V vs. RHE), performed in 0.1 M $HClO_4$ at T = 353 K under inert atmosphere. Before and after these ASTs, the electrocatalysts were characterized in terms of electrochemical surface area (using CO-stripping voltammetry) and oxygen reduction activity (ORR, using linear scan voltammetry) in a dedicated cell. In that case, the electrolyte was 0.1 M $HClO_4$ at T = 298 K and was changed before the post ageing characterizations. Overall, the electrochemical procedures are fully described in Ref. 94.

Physicochemical characterizations.—EPR spectra were acquired with a Bruker EMX digital X band (ν = 9.653 GHz) spectrometer. Diphenylpicrylhydrazil (DPPH) was used as the calibration reference to determine the resonance frequency. To avoid saturation of the cavity, very low sample weights were used, i.e. less than 0.1 mg. The accuracy on weight did not allow the absolute spin density to be estimated.

Nitrogen adsorption isotherms were measured at T = 77 K by a Micromeritics ASAP 2020 automatic apparatus. Before measurements, samples were pre-treated under secondary vacuum at T = 523 K for 12 h for sufficient removal of adsorbed impurities.

The electronic conductivity was investigated by a direct resistance measurement with a cell conceived in-house. 50 mg of material were introduced between two copper electrodes (surface 0.7854 cm^2) surrounded by a Teflon ring. When a pressure of $6.37.10^7$ Pa (0.5 ton) was applied, different currents were applied (−105 mA, 105 mA and 400 mA) with a potentiostat and the value of the tension for each current was recorded. The electronic conductivity σ was calculated as an average of the 3 values obtained with the 3 currents using the formula $\sigma = e.I/U.S$ where e is the thickness of the sample, I the current applied, U the tension measured and S the surface of the electrode.

Raman spectroscopy was used to study the fresh and aged electrocatalysts. The spectra were recorded ex situ using a Renishaw RM1000 spectrometer. The wavelength LASER excitation was λ = 514 nm. For the sake of comparison, the Raman spectra were normalized to the intensity of the graphitic lattice band (at about ν = 1585 cm^{-1}). Curve fitting was performed using the LabSpec software. Mean crystallite size of the carbon particle (lateral extension of the graphite planes) was determined with the Knight and White formula, both for the bare carbon supports and the fluorinated ones, prior to any electrochemistry and for all materials after the ASTs. Overall, the whole procedure is thoroughly described in Ref. 12.

The electrocatalysts Pt content was determined by AAS (PinAACle 900F, PerkinElmer). The electrocatalysts (m = 5 ± 1 mg) were first digested in a 1 mL HCl:HNO_3 3:1 solution made from high-purity acids (37 vol.% ACS Reagent Sigma Aldrich and 65 vol.% Sigma-Aldrich, respectively) for t = 72 h at T = 298 ± 1 K. The solution was then diluted sevenfold to reach the AAS range for Pt and Ni. The wavelength considered for Pt was λ = 266 nm.

The different electrocatalysts were analyzed using a PANalytical X'Pert Pro MDP vertical goniometer/diffractometer equipped with a diffracted-beam monochromator using CuKα radiation (λ = 0.1548 nm) operating at U = 45 kV and I = 40 mA. The 2θ angle extended from 20 to 92° (step size of 0.084°). The X-ray Diffraction

Downloaded on 2018-05-04 to IP 77.158.181.1 address. Redistribution subject to ECS terms of use (see ecsdl.org/site/terms_use) unless CC License in place (see abstract).

Table I. Physicochemical and textural parameters of the various carbon substrates used in the study, either bare or after fluorination. "n.d." stands for not determined. * Imerys Graphite & Carbon reports a value of 770 m^2 g^{-1}. # SN2A reports a value of 110 ± 10 m^2 g^{-1}.

Sample	BET area (m^2 g^{-1})	Carbon particle size (nm)	L_a (nm)	Fluorination (%)	Surface dangling groups (%)	Electronic conductivity (S cm^{-1})
EN	808*	50 ± 10	1.2	0	31	2.6
CA	656	15 ± 5	0.7	0	≈ 100	2.3
YS	126 #	30 ± 10	3.5	0	27	2.9
EN-F-24%	630	40 ± 10	1.3	24	17	0.2
CA-F-25%	519	15 ± 5	0.9	25	97	0.05
YS-F-05%	117	35 ± 10	1.8	5	43	n.d.
YS-F-14%	137	35 ± 10	1.5	14	10	0.1
YS-F-37%	215	35 ± 10	1.3	37	8	n.d.

(XRD) data was used to quantify the average crystallite sizes of the Pt nanoparticles (d_{XRD}) using the Scherrer equation.

The Pt/C nanoparticles were observed using transmission electron microscopy (TEM), realized on a Jeol 2010 microscope equipped with a LaB_6 filament (point-to-point resolution of 0.19 Å). From the micrographs, the isolated nanoparticles of platinum were enumerated, and representative average nanoparticle diameters were calculated (d_N, d_S, d_V, see e.g.[34]).

Results and Discussion

Physicochemical properties of the bare and fluorinated carbons.—The BET surface area of the various carbon supports was measured by nitrogen absorption. The high surface area carbon (Imerys Graphite & Carbon ENSACO 350 G Conductive Carbon Black, hereafter denoted by "EN") features the highest BET area (ca. 800 m^2 $g^{-1}{}_{EN}$, in agreement with the provider's information: 770 m^2 $g^{-1}{}_{EN}$), followed by the in-house-prepared carbon aerogel (hereafter noted "CA", ca. 650 m^2 $g^{-1}{}_{CA}$) and then the commercial graphitized acetylene black (YS, from SN2A: Société du Noir d'Acétylène de l'Aubette, hereafter denoted by "YS", ca. 120 m^2 $g^{-1}{}_{YS}$, in agreement with the provider's information: 110 m^2 $g^{-1}{}_{YS}$). Upon fluorination, the trend is usually that the BET area decreases (Table I), at least when the initial carbon BET area is "large", as already observed by Berthon-Fabry et al.[72] by an enlargement of the pores size; the same proceeds for the YS support when the fluorination rate is small (YS-F-05%). However, for the YS support, high fluorination rates yield increased BET area, the increase scaling with the fluorination rate. This suggests that the porosity of the YS carbon "opens" upon fluorination, in agreement with literature.[95] Hence, fluorination can be assimilated to a decomposition reaction of the YS support by the F_2 precursor, which could be detrimental to the material's stability. This hypothesis will be tested hereafter.

Raman spectroscopy was used to probe the structural properties of the various carbon support materials, and in particular to determine the extent of their graphitization, via the average in-plane crystallite size value: L_a. The initial CA is near-completely amorphous (L_a = 0.74 nm), while YS displays a very graphitic texture (L_a = 3.54 nm). The third sample exhibits intermediate characteristics, (L_a = 1.2 nm), which indicates that EN is essentially a mixture of small graphitic domains separated by amorphous regions, which is typical of the turbostratic structure of high-surface area carbons (see e.g. Ref. 36). The different carbon supports behave in a markedly different manner upon fluorination. For the initially disorganized (poorly-graphitic) carbons, i.e. CA and to a lesser extent EN, fluorination leads to a non-negligible increase of L_a. This feature indicates that the amorphous domains (e.g. the dangling groups of carbon that are a marker of their surface disorder[80,81]) are reacting with the fluorine precursor prior to the more graphitic domains of carbon (Figure 1). In that extent, the fluorination process resembles the initial "corrosion" steps of the carbon support in PEMFC cathode environment: the disordered (non-graphitic) domains of carbon are populated by oxygenated surface groups in priority, and therefore corrode preferentially.[12] Then, in a second step, the graphitic domains are progressively amorphized in water/oxygen-containing media (i.e. typically the operating conditions of a PEMFC cathode) into oxygenated surface groups, which are known to trigger their corrosion. That second process can again be compared to the effect of fluorination of the graphitic carbon: L_a severely decreases from the bare YS to the fluorinated YS-F-x% substrates signing that, in absence of disordered carbon domains, fluorination proceeds by the progressive "unzipping" of the graphitic domains. In consequence, it is observed that the larger the extent of fluorination, the larger the decrease in L_a (Table I). In this case, one can conclude that the fluorination progressively destroys the graphitic domains of the YS carbon to convert them into surface C-F bonds, and then bulk C-F bonds if the extent of fluorination further increases. These findings corroborate the changes of BET area upon fluorination discussed above, and were observed by Guerin et al. in a former study.[95]

The fluorination rate (calculated as the ratio between the F and the C atoms: *Fluorination* = F / C x 100) was measured by weight gain with respect to the initial support in the fluorination oven and are listed in Table I. It was deliberately chosen to have average-high and "comparable" degrees of fluorination for the EN and CA samples (ca. 25%), since these carbons display large BET surface areas. For the graphitic YS carbon, of much smaller BET area, the fluorination was varied from a low (5%) to a high (37%) value, an intermediate value (14%) being also targeted to evaluate whether there exists an optimal extent of fluorination. This latter degree of fluorination has been chosen to make possible a comparison of the behavior of the three types of fluorinated carbons with one another, at a "near-similar" extent of surface-fluorine atoms (EN-F-24% and CA-F-25% samples will be compared with YS-F-14% for that purpose).

The EPR data, some examples of which are presented in Figure 1, are summarized in Table I. CA displays near 100% surface dangling groups, in agreement with (i) the very small size of the CA particles and (ii) their very amorphous behavior (see Raman measurements). To be more specific, the amount of carbon dangling groups of the bare supports more or less scales with the degree of "organization" of the bare substrates: more graphitized carbon supports (the larger L_a) yield smaller proportion of (surface) dangling groups. Upon fluorination, the amount of "free" dangling groups is reduced, since they preferentially react with the fluorine precursors (see Introduction). For a higher degree of fluorination (e.g. YS-F-37%), it is likely that not only the surface dangling groups of carbon are combined with F atoms, but that bulk dangling groups also start being fluorinated. This effect is not desirable, as it destroys the graphitic structure of YS and decreases its electronic conductivity (as indicated in Table I). In essence, heavily-fluorinated carbons exhibit very low values of L_a: here again a parallel can be drawn with the electrochemical corrosion of carbon supports in PEMFC cathode environment during which L_a values are decreasing both in "half-cell"[12,39,44,78,96] and real PEMFC systems.[13,14,97]

Physicochemical characterization of the Pt-based electrocatalysts.—These materials, all presented in Table I, were then used to synthesize carbon-supported nanoparticles. A

Downloaded on 2018-05-04 to IP 77.158.181.1 address. Redistribution subject to ECS terms of use (see ecsdl.org/site/terms_use) unless CC License in place (see abstract).

Table II. Physicochemical and textural parameters of the various Pt/C electrocatalysts. The Pt wt% were calculated at ± 1% and the average nanoparticles diameter at ca. ± 0.2 nm (see Figure S6 for the XRD pattern of the YS-F-05%).

Sample	Pt content (wt% - AAS)	d_N (nm)	d_S (nm)	d_V (nm)	d_{XRD} (nm)
EN	32.7	2.4	3.1	3.5	2.3
CA	36.8	2.2	2.6	2.9	2.0
YS	30.9	2.2	2.4	2.5	2.6
EN-F-24%	37.5	2.6	3.1	3.4	2.8
CA-F-25%	32.9	2.6	3.4	3.9	2.0
YS-F-05%	38.2	2.4	2.6	3.1	11.2
YS-F-14%	25.2	2.4	2.7	2.9	2.3
YS-F-37%	21.0	2.8	3.1	3.3	2.7

nominal Pt loading of 40 wt% was targeted, and this value was essentially reached for all the samples, as measured by atomic absorption spectrometry (Table II). A similar batch of Pt colloids (prepared by the modified polyol synthesis) was used for Pt deposition at all the different carbon substrates. In this manner, the Pt crystallites shall be identical for all the samples, and the various electrocatalysts differ essentially by their extent of Pt nanoparticles agglomeration but not by their individual Pt nanocrystallite sizes. The latter, determined from XRD spectra using the Scherrer equation, demonstrates that this objective was fulfilled for all the samples (d_{XRD} only varies between 2.0 and 2.8 nm, except for the heavily-fluorinated graphitic carbon, YS-F-37%, for which $d_{XRD} = 3.5$ nm): the individual crystallites of Pt are basically of the same size for all the samples, irrespective of the nature of the carbon support (fluorinated or not) and of the degree of fluorination.

The TEM micrographs of Figure 2 and Figure 3 confirm that, indeed, the size of the isolated Pt nanoparticles was essentially similar. The number-averaged Pt nanoparticles diameter, extracted from particle size distribution on ca. 200 isolated Pt nanoparticles, varies in the range $2.2 < d_N < 2.8$ nm for all the samples, in perfect agreement by the value of d_{XRD} presented above (Table II). However, the Pt nanoparticles are organized differently onto different carbon supports; in particular, different degrees of agglomeration were obtained. In essence, the Pt nanoparticles are more agglomerated for the low-surface area carbon (YS) than for the high-surface area one (EN). The case of the CA is peculiar in the way that, due to the large BET area of this substrate, one would have expected a better dispersion of the Pt nanoparticles and a lower extent of agglomeration, which was not witnessed in Figure 2. This is because CA is a monolithic carbon, hence the "intrusion" of the Pt colloids in the pores is not granted. As a result, most of the Pt nanoparticles are agglomerated on the outer surface of the carbon micro-monoliths, causing this heterogeneous distribution of the Pt nanoparticles. In consequence, it is likely that the core of the micro-monoliths is essentially free of Pt nanoparticles (or at least less populated than the outer surface).

Figure 3 indicates that the presence of C-F groups at the fluorinated carbon surface was of little influence on the Pt nanoparticles dispersion. This differs from the results of Berthon-Fabry et al.,[77] for which the distribution and coverage of the Pt nanoparticles was non-negligibly differing in presence/absence of fluorination, and this probably results from the method used at the time (the deposition of Pt was then performed by a water-in-oil microemulsion method). Apart from the two heavily-fluorinated YS carbon (YS-F-14% and YS-F-37%), for which it is likely that bulk fluorination had occurred, the Pt wt% reached was also not altered by the extent of fluorination (Table II). In addition, the distribution of the Pt nanoparticles at the fluorinated carbon supports appears homogeneous (even if some regions of carbon with little Pt nanoparticles coverage could be, very occasionally, found, in particular for the heavily-fluorinated sample YS-F-37%, and on the opposite very high coverage was found in several regions for YS-F-5%), as is the average extent of agglomeration for a given carbon (fluorinated or not). This means that the main driver

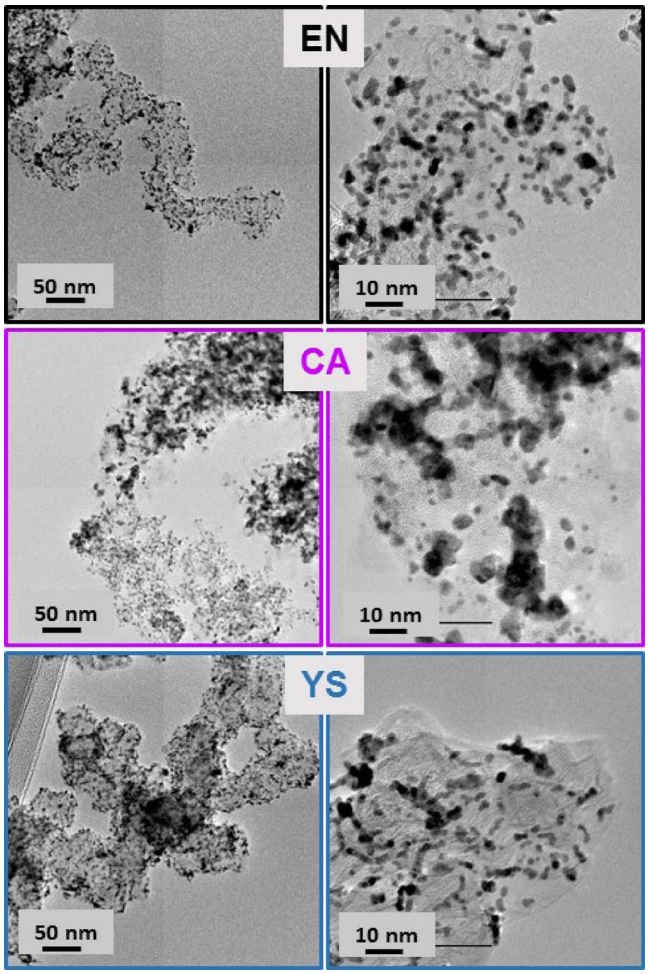

Figure 2. Representative TEM micrographs of the Pt/C nanoparticles deposited at the bare carbon supports, at low (left) and high (right) magnification.

for Pt nanoparticles agglomeration is the available carbon specific surface area and not the local surface chemistry of the substrate. Only for the EN and EN-F-24% samples can this statement be (a little) put into question; the extent of Pt nanoparticles agglomeration seems slightly larger for the fluorinated material than for its bare counterpart. This result may be due to electrostatic repulsions between the fluorinated groups of the carbon support and the negatively charged $PtCl_6^{2-}$ ions used for the Pt nanoparticles synthesis. Favoring attractive interactions between the oxide groups of the carbon support and the Pt salt precursor is the basis of the "Strong Electrostatic Adsorption" (SEA) technique first introduced by Regalbuto and co-workers.[98–100] The authors have shown that the oxide groups present at the carbon surface protonate and positively charge, favoring anion adsorption at pH below the point of zero charge (PZC); conversely anion adsorption is disadvantaged at pH located above the PZC, hence favoring agglomeration of the depositing metal nanoparticles. In summary, the different Pt/C samples differ by their extent of Pt nanoparticles agglomeration, but neither by their Pt wt% and Pt nanoparticles (and crystallite) size.

Electrochemical characterizations in the pristine state (before AST).—These materials were then tested electrochemically, firstly in terms of initial CO_{ads} stripping behavior and of ORR activity in 0.1 M $HClO_4$ electrolyte. A set of representative background-subtracted CO_{ads} stripping voltammograms is presented for the eight Pt/C samples in Figure 4. The CO_{ads} stripping voltammograms features are confirming the results of the physicochemical data: the extent of Pt nanoparticles agglomeration is non-negligible in all cases,

Downloaded on 2018-05-04 to IP 77.158.181.1 address. Redistribution subject to ECS terms of use (see ecsdl.org/site/terms_use) unless CC License in place (see abstract).

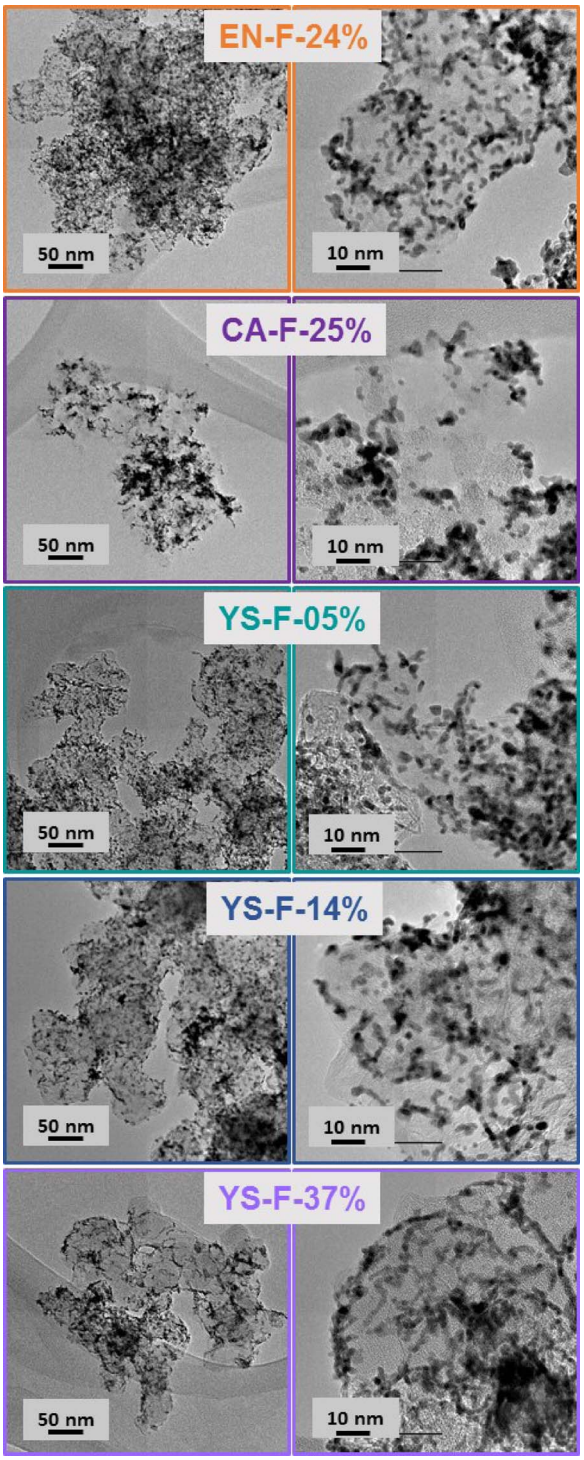

Figure 3. Representative TEM micrographs of the Pt/C nanoparticles deposited at the fluorinated carbon supports, at low (left) and high (right) magnification.

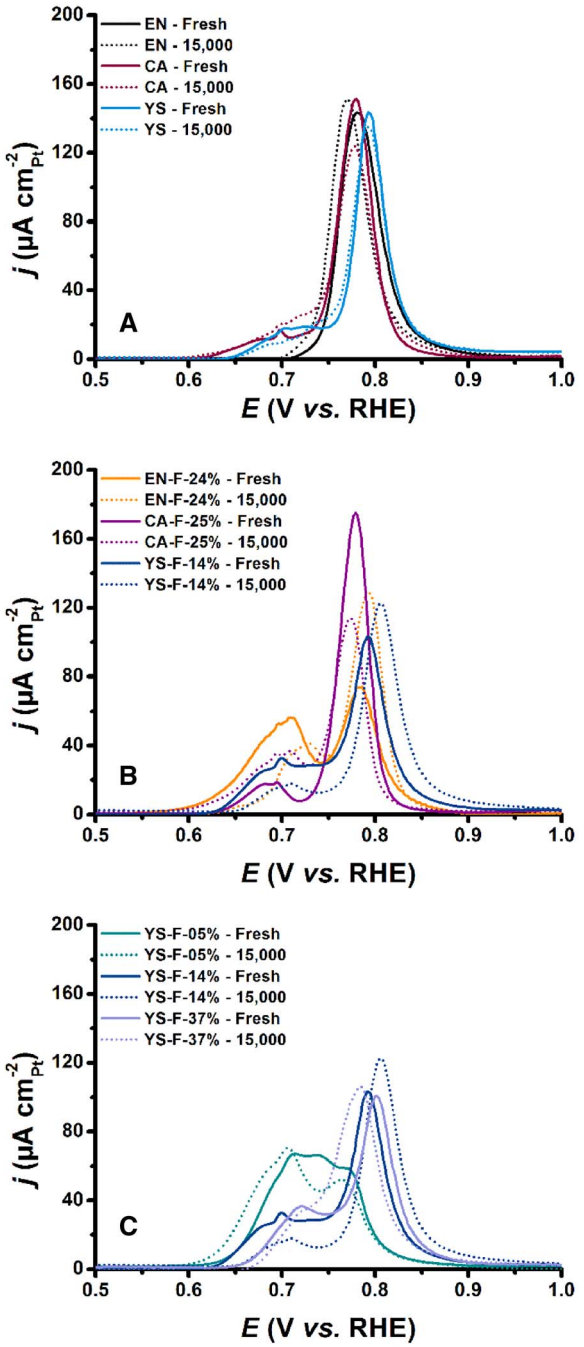

Figure 4. Representative CO_{ads} stripping voltammograms of the various Pt/C samples measured in 0.1 M $HClO_4$ at T = 298 K before (Fresh) and after 15,000 cycles of AST in the range 0.6 < E < 1.0 V vs. RHE in 0.1 M $HClO_4$ at T = 353 K. Comparison of the (A) non-fluorinated EN, CA and YS, (B) average-fluorinated EN, CA and YS and (C) YS with increasing extent of fluorination.

except for the non-fluorinated EN sample, as reveled by the presence of low-potential pre-peak of CO_{ads} stripping in that latter case.[101,102] For the low BET area YS sample and the "poorly-intruded" CA, non-negligible agglomeration of the Pt nanoparticles is confirmed, the extent of which grows upon fluorination. On the contrary, only small differences in terms of (rather symmetric) shape and potential of the main peak of CO_{ads} stripping voltammograms can be observed for the Pt/C electrocatalysts in their pristine state ("Fresh" traces in Figure 4), showing that the Pt nanoparticles are in all case essentially monodisperse (confirming the Pt diameter values of Table II) and comparable for all the samples. The only material that, in occasion, diverges from this trend (and this strongly depends on the electrode characterized, see Figure 6) is the YS-F-05% for which the main CO_{ads} stripping peak is essentially absent, revealing the extremely agglomerated nature of this sample. This agrees with its high Pt wt% and rather heterogeneous nature (regions of the carbon with very high extent of Pt nanoparticles agglomeration and coverage do coexist with other "normally"-populated areas). The electrochemical surface areas of

Downloaded on 2018-05-04 to IP 77.158.181.1 address. Redistribution subject to ECS terms of use (see ecsdl.org/site/terms_use) unless CC License in place (see abstract).

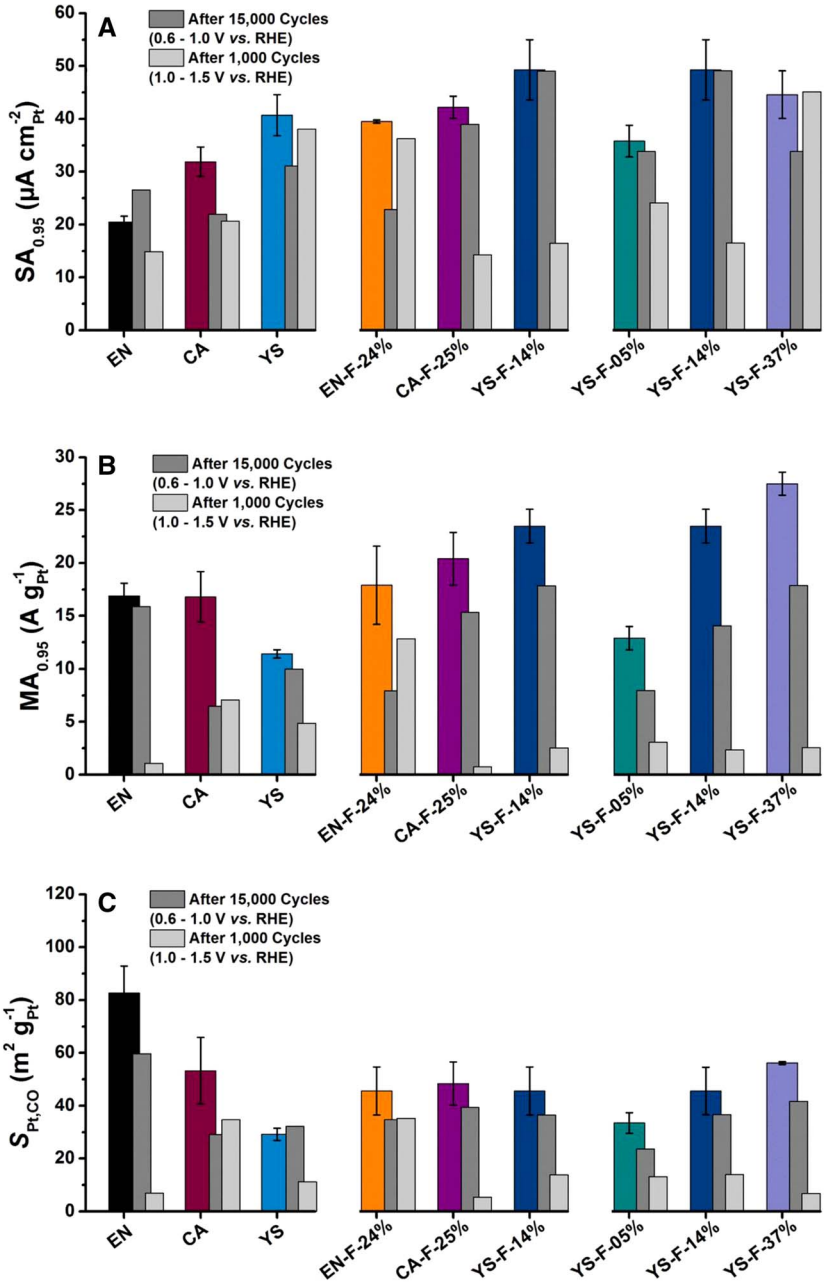

Figure 5. Representative electrochemical properties of the various Pt/C samples measured in 0.1 M $HClO_4$ at T = 25°C before (Fresh) and after 15,000 cycles of AST in the range 0.6 < E < 1.0 V vs. RHE or after 1000 cycles of AST in the range 1.0 < E < 1.5 V vs. RHE in 0.1 M $HClO_4$ at T = 80°C. (A) Specific activity of ORR ($SA_{0.95}$) and (B) mass activity of ORR ($MA_{0.95}$), both parameters being measured after correction of the mass-transport and ohmic-drop limitations at E = 0.95 V vs. RHE. (C) Electrochemical surface areas of platinum ($S_{Pt,CO}$) extracted from the CO-stripping peak coulometry, assuming $Q_{Pt,CO} = 420\ \mu C\ cm^{-2}{}_{Pt}$.

platinum (ECSA, hereafter quantified by $S_{Pt,CO}$) can be extracted from the CO_{ads} stripping coulometry, assuming $Q_{Pt,CO} = 420\ \mu C\ cm^{-2}{}_{Pt}$. These values are reported in Figure 5C and Table III. They essentially confirm the trends brought by the physicochemical characterizations discussed above: for the non-fluorinated carbons, the ECSA scales with the BET surface area of the support (and denotes for the larger extent agglomeration for the low-surface area YS carbon and for the poor penetration of the porosity for the CA). This trend is somewhat leveled for the fluorinated carbons with an average fluorination extent (Figure 5C), as a result from a compromise between the partial

Table III. Summary of the kinetic parameters extracted from the ORR voltammograms for the various Pt/C samples. R_k is the increase of the resistance to the ORR kinetic current upon the start-stop AST.

Sample	$S_{Pt,CO}$ ($m^2\ g_{Pt}{}^{-1}$)	$SA_{0.95}$ ($\mu A\ cm_{Pt}{}^{-2}$)	$MA_{0.95}$ ($A\ g_{Pt}{}^{-1}$)	R_k (Fresh → Start-Stop) ($\Omega\ cm_{Pt}{}^2$)
EN	82.7 ± 10.2	20.5 ± 1.1	16.9 ± 1.2	207 ± 14
CA	53.3 ± 12.6	31.9 ± 2.8	16.8 ± 2.4	190 ± 10
YS	29.2 ± 2.3	40.7 ± 3.9	11.4 ± 0.4	17 ± 02
EN-F-24%	45.6 ± 9.1	39.5 ± 0.3	17.9 ± 3.7	31 ± 01
CA-F-25%	48.4 ± 8.2	42.2 ± 2.1	20.4 ± 2.5	172 ± 09
YS-F-05%	33.5 ± 3.9	35.8 ± 3.0	12.9 ± 1.1	36 ± 02
YS-F-14%	45.6 ± 9.1	49.3 ± 5.7	23.5 ± 1.6	18 ± 01
YS-F-37%	56.2 ± 0.5	44.6 ± 4.5	27.5 ± 1.1	20 ± 01

Downloaded on 2018-05-04 to IP 77.158.181.1 address. Redistribution subject to ECS terms of use (see ecsdl.org/site/terms_use) unless CC License in place (see abstract).

occupation of carbon dangling groups by F atoms (reducing the possibility of Pt nanoparticles stabilization in these regions and therefore decreasing the ECSA for fluorinated amorphous carbons: EN and CA) and the fluorination-induced partial amorphization of the graphitic YS carbon support, which enhances the interaction between the substrate and the Pt nanoparticles. This effect is spectacular and well witnessed in Figure 5C: the higher the fluorination rate, the larger the apparent ECSA and lower the extent of Pt nanoparticles agglomeration (Figure 4C).

The oxygen reduction activity of the pristine Pt/C electrocatalysts (referred to as "Fresh" in what follows) was then evaluated. A representative ORR voltammogram is given in Figure S1 for YS and YS-F-37%. From the ORR characterizations, two important parameters were extracted: the specific activity and the mass activity for the ORR, both measured after correction of the mass-transport and ohmic-drop limitations at $E = 0.95$ V vs. RHE. The corresponding values of specific activity ($SA_{0.95}$) and ($MA_{0.95}$) are displayed in Figure 5A, Figure 5B and Table III, respectively, while the specific activity ($SA_{0.90}$) and mass activity ($MA_{0.90}$) are provided in Table S1.

For the initial bare carbons, $SA_{0.95}$ scales inversely with the ECSA ($S_{Pt,CO}$) and therefore to the BET surface area of the carbon supports ($SA_{0.95}$ decreases in the order YS > CA > EN). It also scales directly with the extent of Pt nanoparticles agglomeration this may be accounted for by the higher ORR activity of interconnected Pt nanoparticles in agglomerates, as recently unveiled by Dubau et al.[103,104] (as here, there is literally no difference of ORR activity to be expected by the so-called Pt nanoparticle size effect mentioned above,[83,84] because the differences of individual crystallite sizes are very small, see Table II). On the contrary, the $MA_{0.95}$ values place the materials in the opposite order ($MA_{0.95}$ decreases in the order EN ≈ CA > YS), due to different $S_{Pt,CO}$ values (Table III). Concerning the average-fluorinated samples, all are more active than their bare carbon equivalents (both in $SA_{0.95}$ and $MA_{0.95}$), in line with the fact that fluorinated carbon surfaces present a non-negligible ORR activity both in acidic[74,75] and alkaline electrolytes.[76] Besides, the larger the fluorination rate, the larger the ORR activity, especially in terms of $MA_{0.95}$.

Durability and electrochemical activity in base-load cycles (15,000 steps for 0.6 < E < 1.0 V vs. RHE).—The Pt/C samples were all submitted to potential cycling in the range $0.6 < E < 1.0$ V vs. RHE, to test their robustness in "base-load" conditions. All the electrocatalysts show a depreciated ECSA after the AST, except YS, for which the slight increase of ORR activity versus the Fresh state is within the error bar (Figure 5C). These results confirm that the extent of graphitization has a very negligible influence on the degradation of the electrocatalysts in the $0.6 < E < 1.0$ V vs. RHE potential range, as previously reported in Refs. 12, 39. However, it is worth noting that the load-cycle protocol resulted in a minor corrosion of the non-graphitized part of the carbon support, as evidenced by the increase of L_a (determined from the Raman spectrum presented in Figure S4A, see Table IV) for all carbon support except YS (i.e. the already graphitized carbon), which can be accounted for by a diminution of the density of non-graphitized domains in the carbon support.

In terms of ORR activity, except for EN, for which a slight improvement of $SA_{0.95}$ is noted (because of the higher agglomeration of Pt nanoparticles), all the $SA_{0.95}$ and $MA_{0.95}$ values do depreciate upon the base-load protocol. This depreciated ORR mass activity essentially originates from the decrease in $S_{Pt,CO}$ in these conditions, mostly associated to Ostwald ripening and the Pt-catalyzed carbon support corrosion.[12,39] Indeed, the Pt nanoparticles are rounder and larger after the base-load protocol (see the representative TEM micrographs of Figure S2 and Figure S3) than they were before (see Figure 2 and Figure 3). However, their extent of agglomeration does not increase sharply upon the AST, which agrees with former report[39] that the base-load protocol is not the most aggressive to the carbon support material. To summarize, the base-load protocol mildly degraded the Pt/C nanoparticles. They essentially undergo significant growth of Pt mean diameter according to Ostwald ripening[88,105] and very minor agglomeration due to moderate carbon corrosion. In these conditions, the non-negligible $S_{Pt,CO}$ loss is counterbalanced by the gain in specific activity associated with the growth of the nanoparticles, resulting in moderate decrease in mass activity. Because the carbon supports are (slightly) corroding in a process that is catalyzed by Pt nanoparticles, there are almost no differences in the fate of the Pt/C electrocatalysts, whatever their initial degree of graphitization or their (rate of) fluorination.

Table IV. Changes in the average in-plane crystallite size of the carbon (L_a) for the various carbon support discussed in this work, after the load-cycle (15,000 cycles between 0.6 and 1.0 V vs. RHE at 50 mV/s) and the start-stop (1,000 square cycles between 1.0 and 1.5 V vs. RHE) protocols.

	L_a (nm)		
	Fresh	load-cycle	start-stop
EN	1.2	1.5	1.7
CA	0.7	3.3	1.8
YS	3.5	3.6	2.0
EN-F-24%	1.3	1.7	1.7
CA-F-25%	0.9	1.4	1.9
YS-F-05%	1.8	2.6	2.1
YS-F-14%	1.5	1.9	1.6
YS-F-37%	1.3	2.0	2.0

Durability and electrochemical activity in start-stop cycles (1,000 steps for 1.0 < E < 1.5 V vs. RHE).—The picture clearly changes when the AST is more severe toward the carbon supports, i.e. for the start-stop AST protocol, (1,000 three-second potential steps for $1.0 < E < 1.5$ V vs. RHE).

Bare carbon substrates.—When one looks at the voltammograms in supporting electrolyte, a change of the double layer capacitance can be noticed for $0.3 < E < 0.5$ V vs. RHE (Figure 6A): (i) the EN quinone-hydroquinone features undergo a dramatic decrease in electrical charge, the latter being associated to a severe drop of the response of the Pt-hydrogen and Pt-oxide features, sign of an intense degradation of this electrocatalyst. (ii) The CA and the YS suffer from similar losses in ORR mass activity and specific surface area. This is surprising considering the amorphous nature of the CA but, while looking at the Figure 6A, one can see that the charge under the quinone-hydroquinone peak increases, this being significant for an incomplete corrosion of the carbon support ($C \rightarrow CO_{surf}$), by opposition to the complete oxidation observed on EN. These differences can be ascribed to the fact that for CA, most of the Pt nanoparticles are located on the outer-surface of the carbon micromonoliths, which leaves substantial carbon surface "free" of Pt, and therefore prone to surface functionalization (and not complete corrosion), which is a different situation than for the EN sample (where most of the carbon surface is covered with Pt nanoparticles and therefore corroded entirely in the load-cycle protocol). The YS carbon resistance to this AST is much higher than observed for EN, in line with the better ability of graphitic carbon supports to withstand corrosion at high electrode potential.[12,39] However, the diminution in L_a observed for the YS carbon during the start-stop protocol (L_a (fresh) = 3.5 nm vs. L_a (aged) = 2.0 nm, see Table IV) is accounted for by the creation of structural defects into its graphitic domains, i.e. their corrosion.

Figure 7 enables going further in the analysis of the ORR activity before/after AST P2. Figure 7E presents the variation of ΔR_k, i.e. the changes in resistance induced by the degradation in the carbon support during the ageing, determined from Figure 7A for the bare carbons. Indeed, in the discussed potential range, the potential difference (ΔE) between the LSVs presented in Figure 7A before and after the start-stop protocol evolves linearly with j_k. Such linearity suggests an increase in the resistance of the system (R_{tot}), the latter corresponding to the sum of (i) the resistance of the electrolyte (R_{el}),

Downloaded on 2018-05-04 to IP 77.158.181.1 address. Redistribution subject to ECS terms of use (see ecsdl.org/site/terms_use) unless CC License in place (see abstract).

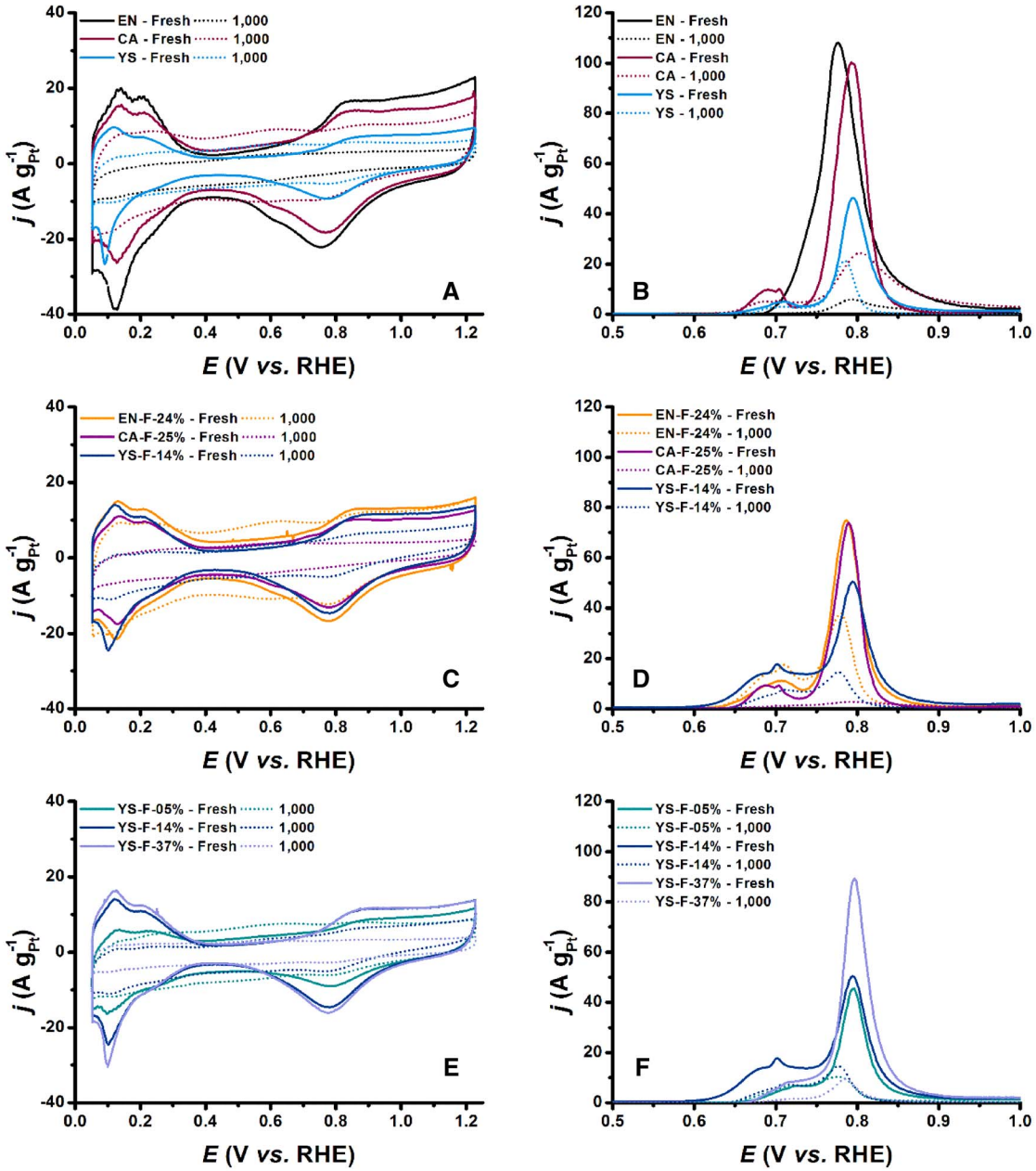

Figure 6. (A, C and E) Representative voltammograms of the various Pt/C samples monitored in supporting electrolyte before (Fresh) and after 1,000 cycles of start-stop protocol AST (1,000 three-second steps for 1.0 < E < 1.5 V vs. RHE in 0.1 M $HClO_4$ at T = 353 K); (B, D and F) Representative CO-stripping voltammograms of the various Pt/C samples measured in 0.1 M $HClO_4$ at T = 298 K before (Fresh) and after 1,000 cycles of start-stop AST. (A, B) bare carbons, (C, D) average-fluorinated carbons and (E, F) YS carbon with three different levels of fluorination.

of (ii) the glassy carbon (R_{GC}) and of (iii) the catalytic layer (R_k – see Figure 7D).[106–110] R_{el} of ca. 20 Ω were determined by electrochemical impedance spectroscopy (EIS) before and after the start-stop ageing and R_{GC} was assumed to be negligible, owing to the high electronic conductivity of the glassy carbon. Therefore, the resistance variations (ΔR_k) measured for the various electrocatalysts in Figure 7 were essentially associated with the resistance of the catalytic layer, which is composed of the internal resistance of the carbon grains, R_{gr}, the resistance induced by the oxide groups onto the carbon surface (ex. the quinone/hydroquinone species, R_{HQ}) and the resistance of the carbon grain boundaries (R_{cx}). Thus, the increase of R_k (i.e. $\Delta R_k > 0$) during the start stop AST corresponds to the degradation of the carbon support, likely by (i) the formation of the quinone/hydroquinone oxide layer onto the carbon surface[36,78] and/or (ii) the amorphization of the carbon support, especially in the interconnection regions between the carbon grains, both phenomena resulting in an increase of the carbon support resistance.[110] All bare carbons (EN, CA and YS) featured a positive variation of ΔR_k, while being much lower for the YS than the EN and CA. This is not surprising considering that YS is a graphitized carbon and, as such, is much more resistant to corrosion in the 1.0–1.5 V vs. RHE potential range.[39] It is however surprising that, without noticeable degradation of the YS carbon support ($\Delta R_k = 17 \pm 2\ \Omega\ cm_{Pt}^{-2}$), the latter loses ca. 65% of its Pt specific surface during the P2 ageing (see Figure 5C, left). This can be explained by a weak binding of the Pt nanoparticles onto the surface and, as such, their detachment during the start-stop AST and/or a localized corrosion of the carbon support around the Pt nanoparticles, resulting in dramatic ECSA losses while the overall carbon structure remains essentially intact. An elegant strategy based on space-confinement of the Pt nanoparticles into the pores of hollow graphitic spheres was

Downloaded on 2018-05-04 to IP 77.158.181.1 address. Redistribution subject to ECS terms of use (see ecsdl.org/site/terms_use) unless CC License in place (see abstract).

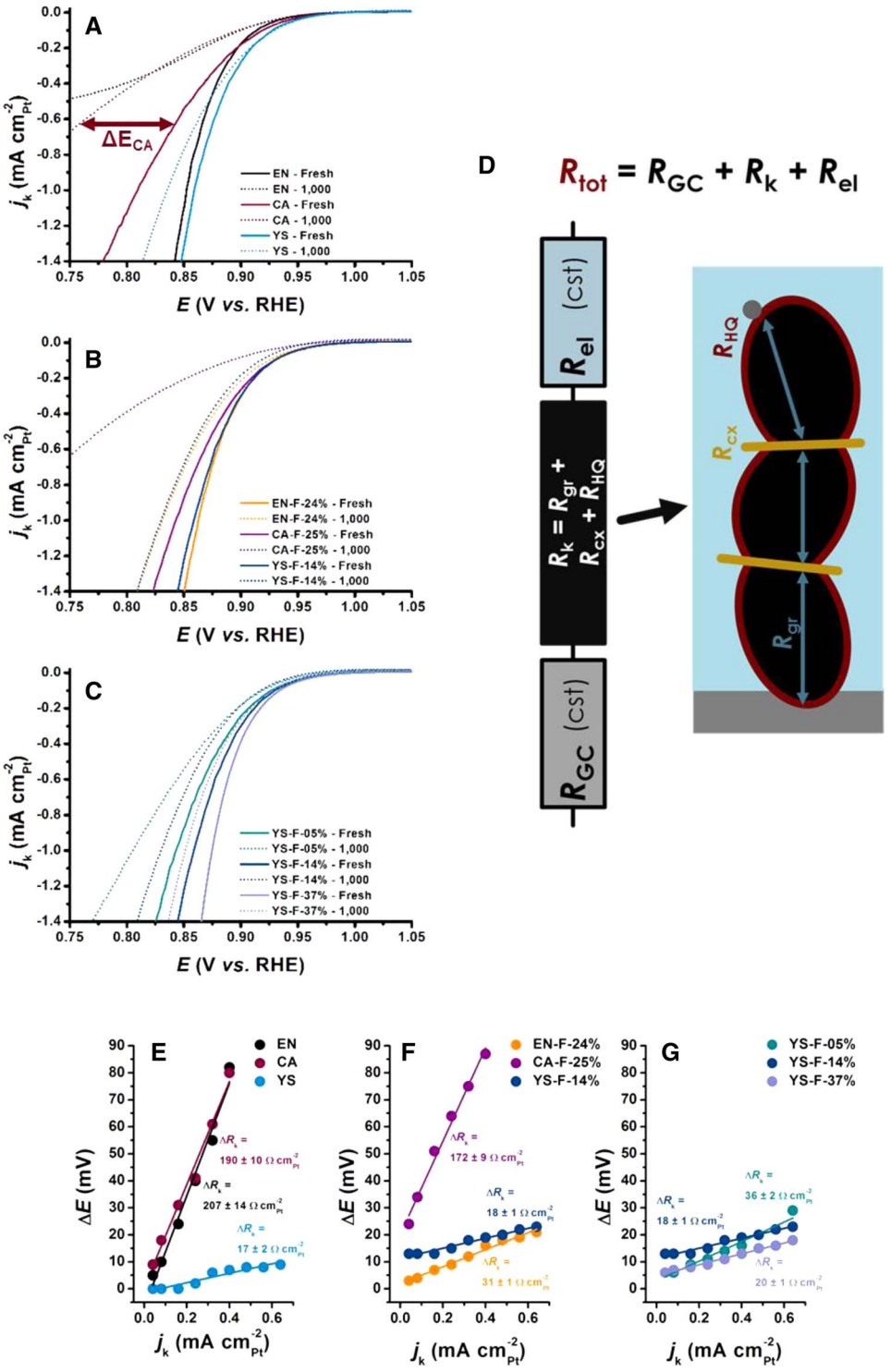

Figure 7. (A-C) Representative ORR voltammograms of the various Pt/C samples measured in 0.1 M $HClO_4$ at T = 298 K before (Fresh) and after 1,000 cycles of start-stop AST, normalized by the specific surface area of the electrocatalysts measured by CO_{ads} stripping and corrected from the diffusion in solution and the ohmic losses. (D) Schematic representation of the nature of R_k, R_{GC} being the resistance of the glassy carbon, R_{el} the resistance of the electrolyte, R_{gr} the resistance inside the carbon grain, R_{cx} the resistance at the carbon grain boundaries and R_{HQ} the resistance induced by the carbon oxide layer. (E-G) Variation in the resistance of the catalytic layer before and after 1,000 cycles of start-stop AST, extracted from Figures 7A–7C for the various Pt/C samples. The y-axis corresponds to the difference in potential at a given current density for the LSVs in O_2-saturated electrolyte before and after the start-stop AST (see A). The ORR measurement were performed in 0.1 M $HClO_4$ at T = 298 K for the (A) bare carbons, (B) the average-fluorinated carbons and (C) the YS sample at different rates of fluorination.

recently proposed by Galeano, Pizzutilo et al.[111,112] to prevent their agglomeration/detachment under these operating conditions, and such strategy could prove adequate in the case of graphitized supports like YS.

Fluorinated carbon substrates.—When the CA, EN and YS carbons are fluorinated, the picture changes. The Pt features almost completely vanished after the start-stop AST for CA-F-25% (Figures 6C and 6D), showing that fluorination is not a solution to protect this carbon. This means that, even if C-F groups are stronger than C-O groups in principle, they cannot insure the total protection of a completely amorphous carbon support. It is wise stating here that, as CA has the smallest carbon particles size and smallest degree of graphitization (Table I), it is likely that its extent of fluorination (25%) was not enough to completely protect the micro-monoliths of CA and/or to populate all the carbon surface dangling groups (in agreement with the data of Table I). In turn, this endangered even more its non-protected (non-fluorinated) regions (that are already very sensitive to high-potential corrosion), that could have acted as "sacrificial anodes" in the carbon corrosion process. As a result, the ORR activity for the CA-F-25% completely vanishes upon AST P2 (Figure 7B and Figure 7F). Furthermore, the variations of R_k during the P2 AST are

Downloaded on 2018-05-04 to IP 77.158.181.1 address. Redistribution subject to ECS terms of use (see ecsdl.org/site/terms_use) unless CC License in place (see abstract).

almost identical for the carbon aerogel before and after fluorination (i.e. $\Delta R_k = 190 \pm 10\ \Omega\ cm_{Pt}^{-2}$ and $\Delta R_k = 172 \pm 9\ \Omega\ cm_{Pt}^{-2}$, respectively), meaning that the carbon support suffers from similar degradation whether it is fluorinated or not.

In opposition, the EN carbon support seems rather well protected by an average fluorination rate (EN-F-24%). Even if a slight increase of carbon oxide groups is noticed in the double-layer region of the voltammograms of Figure 6C, the ECSA is clearly maintained to a non-negligible extent (Figure 6D), which demonstrates the much better stability of EN-F-24% versus EN. This improvement of the EN stability by fluorination during start-stop AST is especially striking while considering the changes in ΔR_k, i.e. $\Delta R_k = 207 \pm 14\ cm_{Pt}^{-2}$ before fluorination and $\Delta R_k = 31 \pm 1\ cm_{Pt}^{-2}$ after fluorination. This signs that the C-F bonds in fluorinated EN-F-24% are stronger than the C-O bonds that were present in the amorphous regions of its non-fluorinated analogue. Combined to the presence of non-negligible amount of graphitic regions in EN (Table I), the C-F bonds present at its surface make of EN-F-24% a rather robust material upon aging in start-stop AST. As a result, the ORR activity of EN-F-24% maintains at a very interesting level (Figure 6H and Figure 7B). To be more specific, the EN-F-24% sample maintains its ORR activity upon AST as well as the graphitized carbon YS did (see Figure 7B), but with the clear advantage to maintain a good dispersion of Pt nanoparticles owing to the much higher BET surface area of the EN-based carbon than for YS.

The YS graphitized carbon support shows an intermediate behavior between EN and CA; its durability is not improved by 14% fluorination, and even is slightly degraded in terms of retained $S_{Pt,CO}$ and even more in terms of ORR activity (Figure 5, Figure 6, Figure 7 and Table III). As explained in the previous section relative to the fluorination, binding fluorine atoms to a graphitic carbon implies that, firstly, some disorder must be brought to the structure: C-C bonds must be broken, since there is a very limited number of surface dangling groups available, as a result of (i) the low initial BET surface area of YS and (ii) of the small rate of surface dangling groups (Table I). The present results show that, although this does not modify the fate of the YS-supported electrocatalysts in the load-cycle AST (where the carbon support chemistry/texture has a little influence on the rate and nature of degradations), it severely depreciates the resistance of its surface to corrosion during the start-stop AST. The overall carbon support resistance does not dramatically increase during the start-stop AST (i.e. a similar increase than without fluorination: $\Delta R_k = 36 \pm 2\ \Omega\ cm_{Pt}^{-2}$ *vs.* up to. $\Delta R_k = 17 \pm 2\ \Omega\ cm_{Pt}^{-2}$ for YS, see Figure 7), meaning that all the ECSA losses occurs through localized corrosion at the nanoparticles/support interface. This is a clear sign that C-C bonds in graphitic regions are more stable than C-F regions in fluorinated carbons. Changing the rate of fluorination for YS has little effect regarding the durability of YS-based Pt/C samples, both on the retention of $S_{Pt,CO}$ (Figure 5 and Table III) and on the rate of ORR activity loss (Figure 7 and Table III). As a result, the larger initial ORR mass activity of fluorinated-YS samples versus YS do not maintain after the start-stop protocol (for the specific activities, having a high degree of fluorination seems more beneficial than a low degree of fluorination, but this does not render the materials more durable than their non-fluorinated YS analogue).

To summarize, the start-stop protocol of AST severely degraded the Pt/C nanoparticles. While they do not undergo significant growth of mean diameter according to Ostwald ripening (because they are passivated by a layer of Pt-oxides and because redeposition of Pt^{z+} ions is not favored in this potential domain), they undergo major agglomeration and detachment following severe carbon corrosion in this potential region.[12,39,113,114] In these conditions, the non-negligible ECSA losses cannot be counterbalanced by any growth of the nanoparticles (which was the case for AST P1), resulting in severe decrease in ORR mass activity. Besides, all the bare carbon supports are corroding in a very important extent. Unlike the load cycle protocol, there is a large difference in robustness for the bare and fluorinated EN carbons, the latter presenting a higher stability than the graphitized YS. CA is however no more stable after fluorination, as YS, which even seems destabilized by the fluorination, owing to the fact that this process initiates its amorphization, a detrimental feature regarding corrosion-resistance in the high potential domain.

Conclusions

Various carbon supports featuring different texture and structure were fluorinated and used as supports to deposit Pt nanoparticles via a modified polyol route. The electrocatalytic activity for the oxygen reduction reaction and the stability of the resulting electrocatalysts were investigated in conditions simulating potential variations at a PEMFC cathode during load cycling ($0.6 < E < 1.0$ V vs. RHE) or start-up/shutdown ($1.0 < E < 1.5$ V vs. RHE). The load cycling protocol caused dissolution/redeposition of the Pt nanocrystallites via Ostwald ripening but led to mild and similar electrochemically active surface area (ECSA) losses and ORR activity for the Pt/raw or fluorinated carbon supports. In contrast, the bare carbon supports were strongly corroded after the start-up/shutdown protocol, resulting in pronounced detachment of the Pt nanocrystallites but no growth in their size (because they are passivated by a layer of Pt-oxides and because redeposition is not favored in this potential domain). However, different fates were observed for fluorinated structurally-ordered and structurally-disordered carbon supports in these conditions: fluorination revealed beneficial for the structurally-disordered carbon supports (carbon black, EN) but not for the structurally ordered one (graphitic carbon, YS). This was rationalized by considering that "free" dangling groups of carbon supports, which are preferentially oxidized in PEMFC cathode environment, react with the fluorine precursors and thus become less prone to oxidation. In contrast, fluorination of structurally-ordered (graphitic) carbon supports creates structural disorder (C-C bond are broken during the process) and depreciates their resistance to electrochemical corrosion. These findings open for the first time the possibility to achieve simultaneously a balance between high carbon specific surface area (hence high Pt dispersion) and limited carbon corrosion under automotive PEMFC conditions.

Acknowledgments

The authors thank the French National Research Agency program (ANR-14-CE05-0047 project CORECAT) for the funding, Capenergies and Tenerrdis for their support and Imerys Graphite & Carbon and SN2A for their kind supply of ENSACO 350 G and YS respectively. This work was performed within the framework of the Centre of Excellence of Multifunctional Architectured Materials "CEMAM" n° AN-10-LABX-44-01. MC thanks the French IUF for its support.

ORCID

Frédéric Maillard https://orcid.org/0000-0002-6470-8900
Marian Chatenet https://orcid.org/0000-0002-9673-4775

References

1. M. S. Wilson and S. Gottesfeld, *J. Appl. Electrochem.*, **22**, 1 (1992).
2. M. S. Wilson and S. Gottesfeld, *J. Electrochem. Soc.*, **139**, L28 (1992).
3. S. Mukerjee, S. Srinivasan, and A. J. Appleby, *Electrochim. Acta*, **38**, 1661 (1993).
4. S. Hirano, J. Kim, and S. Srinivasan, *Electrochim. Acta*, **42**, 1587 (1997).
5. P. Costamagna and S. Srinivasan, *J. Power Sources*, **102**, 253 (2001).
6. P. Costamagna and S. Srinivasan, *J. Power Sources*, **102**, 242 (2001).
7. H. A. Gasteiger, W. Vielstich, and H. Yokokawa, *Handbook of Fuel Cells*, JohnWiley & Sons (2003).
8. H. A. Gasteiger, W. Vielstich, and H. Yokokawa, *Handbook of Fuel Cells*, John Wiley & Sons Ltd, Chichester (2009).
9. L. M. Roen, C. H. Paik, and T. D. Jarvi, *Electrochem. Solid-State Lett.*, **7**, A19 (2004).
10. E. Guilminot, A. Corcella, F. Charlot, F. Maillard, and M. Chatenet, *J. Electrochem. Soc.*, **154**, B96 (2007).
11. N. Takeuchi and T. F. Fuller, *J. Electrochem. Soc.*, **155**, B770 (2008).
12. L. Castanheira, L. Dubau, M. Mermoux, G. Berthomé, N. Caqué, E. Rossinot, M. Chatenet, and F. Maillard, *ACS Catal.*, **4**, 2258 (2014).

Downloaded on 2018-05-04 to IP 77.158.181.1 address. Redistribution subject to ECS terms of use (see ecsdl.org/site/terms_use) unless CC License in place (see abstract).

13. L. Dubau, L. Castanheira, M. Chatenet, F. Maillard, J. Dillet, G. Maranzana, S. Abbou, O. Lottin, G. De Moor, A. El Kaddouri, C. Bas, L. Flandin, E. Rossinot, and N. Caqué, *Int. J. Hydrogen Energy*, **39**, 21902 (2014).
14. L. Dubau, L. Castanheira, F. Maillard, M. Chatenet, O. Lottin, G. Maranzana, J. Dillet, A. Lamibrac, J. C. Perrin, E. Moukheiber, A. Elkaddouri, G. De Moor, C. Bas, L. Flandin, and N. Caqué, *Wiley Interdiscip. Rev.: Energy Environ.*, **3**, 540 (2014).
15. M. Pourbaix, in, p. 453, *National Association of Corrosion Engineers, Houston* (1979).
16. J. Willsau and J. Heitbaum, *J. Electroanal. Chem.*, **161**, 93 (1984).
17. E. Passalacqua, P. L. Antonucci, M. Vivaldi, A. Patti, V. Antonucci, N. Giordano, and K. Kinoshita, *Electrochim. Acta*, **37**, 2725 (1992).
18. F. Maillard, A. Bonnefont, and F. Micoud, *Electrochem. Commun.*, **13**, 1109 (2011).
19. N. Linse, L. Gubler, G. G. Scherer, and A. Wokaun, *Electrochim. Acta*, **56**, 7541 (2011).
20. J. Speder, A. Zana, I. Spanos, J. J. K. Kirkensgaard, K. Mortensen, and M. Arenz, *Electrochem. Com.*, **34**, 153 (2013).
21. W. R. Baumgartner, P. Parz, S. D. Fraser, E. Wallnofer, and V. Hacker, *J. Power Sources*, **182**, 413 (2008).
22. G. Maranzana, C. Moyne, J. Dillet, S. Didierjean, and O. Lottin, *J. Power Sources*, **195**, 5990 (2010).
23. S. Von Dahlen, G. G. Scherer, A. Wokaun, and I. A. Schneider, in *ECS Trans*., p. 1365 (2010).
24. S. Von Dahlen and I. A. Schneider, *Fuel Cells*, **12**, 1004 (2012).
25. J. Durst, A. Lamibrac, F. Charlot, J. Dillet, L. F. Castanheira, G. Maranzana, L. Dubau, F. Maillard, M. Chatenet, and O. Lottin, *Appl. Catal. B*, **138–139**, 416 (2013).
26. A. Oyarce, E. Zakrisson, M. Ivity, C. Lagergren, A. B. Ofstad, A. Bodén, and G. Lindbergh, *J. Power Sources*, **254**, 232 (2014).
27. S. Abbou, J. Dillet, G. Maranzana, S. Didierjean, and O. Lottin, *J. Power Sources*, **340**, 419 (2017).
28. S. Abbou, J. Dillet, G. Maranzana, S. Didierjean, and O. Lottin, *J. Power Sources*, **340**, 337 (2017).
29. J. Xie, D. L. Wood, K. L. More, P. Atanassov, and R. L. Borup, *J. Electrochem. Soc.*, **152**, A1011 (2005).
30. R. L. Borup, J. R. Davey, F. H. Garzon, D. L. Wood, and M. A. Inbody, *J. Power Sources*, **163**, 76 (2006).
31. R. Borup and et al., *Chem. Rev.*, **107**, 3904 (2007).
32. L. Dubau, L. Castanheira, G. Berthomé, and F. Maillard, *Electrochim. Acta*, **110**, 273 (2013).
33. J. Dillet, D. Spernjak, A. Lamibrac, G. Maranzana, R. Mukundan, J. Fairweather, S. Didierjean, R. L. Borup, and O. Lottin, *J. Power Sources*, **250**, 68 (2014).
34. E. Guilminot, A. Corcella, M. Châtenet, F. Maillard, F. Charlot, G. Berthomé, C. Iojoiu, J.-Y. Sanchez, E. Rossinot, and E. Claude, *J. Electrochem. Soc.*, **154**, B1106 (2007).
35. K. Kinoshita and J. Bett, *Carbon*, **11**, 237 (1973).
36. K. Kinoshita, *Carbon: Electrochemical and Physicochemical Properties*, John Wiley & Sons, New York (1988).
37. E. Yli-Rantala, A. Pasanen, P. Kauranen, V. Ruiz, M. Borghei, E. Kauppinen, A. Oyarce, G. Lindbergh, C. Lagergren, M. Darab, S. Sunde, M. Thomassen, S. Ma-Andersen, and E. Skou, *Fuel Cells*, **11**, 715 (2011).
38. S. J. Ashton and M. Arenz, *J. Power Sources*, **217**, 392 (2012).
39. L. Castanheira, W. O. Silva, F. H. B. Lima, A. Crisci, L. Dubau, and F. Maillard, *ACS Catal.*, **5**, 2184 (2015).
40. T. Kim, T. Xie, W. Jung, F. Gadala-Maria, P. Ganesan, and B. N. Popov, *J. Power Sources*, **273**, 761 (2015).
41. T. Xie, W. Jung, T. Kim, P. Ganesan, and B. N. Popov, *J. Electrochem. Soc.*, **161**, F1489 (2014).
42. W. Jung, T. Xie, T. Kim, P. Ganesan, and B. N. Popov, *Electrochim. Acta*, **167**, 1 (2015).
43. M. Watanabe and S. Motoo, *J. Electroanal. Chem.*, **60**, 267 (1975).
44. L. Castanheira, L. Dubau, and F. Maillard, *Electrocatalysis*, **5**, 125 (2014).
45. A. Ohma, K. Shinohara, A. Iiyama, T. Yoshida, and A. Daimaru, *Membrane and Catalyst Performance Targets for Automotive Fuel Cells by FCCJ Membrane*, Catalyst, MEA WG, in *220th ECS Meeting*, p. 775, ECS (2011).
46. T. U. D. O. Energy, *Fuel Cell Technologies Office Multi-Year Research*, Development, and Demonstration Plan, in (2012).
47. D. H. Lim, W. J. Lee, N. L. Macy, and W. H. Smyrl, *Electrochem. Solid-State Lett.*, **12**, B123 (2009).
48. A. Masao, S. Noda, F. Takasaki, K. Ito, and K. Sasaki, *Electrochem. Solid-State Lett.*, **12**, B119 (2009).
49. K. Sasaki, F. Takasaki, Z. Noda, S. Hayashi, Y. Shiratori, and K. Ito, *ECS Trans*., **33**, 473 (2010).
50. M. Wesselmark, B. Wickman, C. Lagergren, and G. Lindbergh, *Electrochim. Acta*, **55**, 7590 (2010).
51. F. Takasaki, S. Matsuie, Y. Takabatake, Z. Noda, A. Hayashi, Y. Shiratori, K. Ito, and K. Sasaki, *J. Electrochem. Soc.*, **158**, B1270 (2011).
52. Y. Ishigami, K. Takada, H. Yano, J. Inukai, M. Uchida, Y. Nagumo, T. Hyakutake, H. Nishide, and M. Watanabe, *J. Power Sources*, **196**, 3003 (2011).
53. I. Cerri, T. Nagami, J. Davies, C. Mormiche, A. Vecoven, and B. Hayden, *Int. J. Hydrogen Energy*, **38**, 640 (2013).
54. Y. Takabatake, Z. Noda, S. M. Lyth, A. Hayashi, and K. Sasaki, *Int. J. Hydrogen Energy*, **39**, 5074 (2014).
55. E. Fabbri, A. Pătru, A. Rabis, R. Kötz, and T. J. Schmidt, *Chimia*, **68**, 217 (2014).
56. E. Fabbri, A. Rabis, R. Kötz, and T. J. Schmidt, *Phys. Chem. Chem. Phys.*, **16**, 13672 (2014).
57. A. Rabis, D. Kramer, E. Fabbri, M. Worsdale, R. Kötz, and T. J. Schmidt, *J. Phys. Chem. C*, **118**, 11292 (2014).
58. G. Ozouf and C. Beauger, *J. Mater. Sci.*, **51**, 5305 (2016).
59. G. Cognard, G. Ozouf, C. Beauger, G. Berthomé, D. Riassetto, L. Dubau, R. Chattot, M. Chatenet, and F. Maillard, *Appl. Catal. B*, **201**, 381 (2017).
60. G. Cognard, G. Ozouf, C. Beauger, L. Dubau, M. López-Haro, M. Chatenet, and F. Maillard, *Electrochim. Acta*, **245**, 993 (2017).
61. G. Cognard, G. Ozouf, C. Beauger, I. Jiménez-Morales, S. Cavaliere, D. Jones, J. Rozière, M. Chatenet, and F. Maillard, *Electrocatalysis*, **8**, 51 (2017).
62. A. Kumar and V. K. Ramani, *Appl. Catal. B*, **138–139**, 43 (2013).
63. A. Kumar and V. Ramani, *ACS Catal.*, **4**, 1516 (2014).
64. M. K. Debe, A. K. Schmoeckel, G. D. Vernstrorn, and R. Atanasoski, *J. Power Sources*, **161**, 1002 (2006).
65. A. Bonakdarpour, K. Stevens, G. D. Vernstrom, R. Atanasoski, A. K. Schmoeckel, M. K. Debe, and J. R. Dahn, *Electrochim. Acta*, **53**, 688 (2007).
66. A. Kongkanand, Z. Liu, I. Dutta, and F. T. Wagner, *J. Electrochem. Soc.*, **158**, B1286 (2011).
67. M. Toupin and D. Bélanger, *Langmuir*, **24**, 1910 (2008).
68. P. Urchaga, M. Weissmann, S. Baranton, T. Girardeau, and C. Coutanceau, *Langmuir*, **25**, 6543 (2009).
69. G. Inzelt, M. Pineri, J. W. Schultze, and M. A. Vorotyntsev, *Electrochim. Acta*, **45**, 2403 (2000).
70. Z. Qi and P. G. Pickup, *Chem. Commun.*, 2299 (1998).
71. G. Nanse, E. Papirer, P. Fioux, F. Moguet, and A. Tressaud, *Carbon*, **35**, 175 (1997).
72. Y. S. Wu, Y. H. Lee, Z. W. Yang, Z. Z. Guo, and H. C. Wu, *J. Phys. Chem. Solids*, **69**, 376 (2008).
73. H. Groult, T. Nakajima, L. Perrigaud, Y. Ohzawa, H. Yashiro, S. Komaba, and N. Kumagai, *J. Fluorine Chem.*, **126**, 1111 (2005).
74. X. Sun, Y. Zhang, P. Song, J. Pan, L. Zhuang, W. Xu, and W. Xing, *ACS Catal.*, **3**, 1726 (2013).
75. H. Wang and A. Kong, *Mater. Lett.*, **136**, 384 (2014).
76. X. Sun, P. Song, T. Chen, J. Liu, and W. Xu, *Chem. Commun.*, **49**, 10296 (2013).
77. S. Berthon-Fabry, L. Dubau, Y. Ahmad, K. Guerin, and M. Chatenet, *Electrocatalysis*, **6**, 521 (2015).
78. Z. Zhao, L. Castanheira, L. Dubau, G. Berthomé, A. Crisci, and F. Maillard, *J. Power Sources*, **230**, 236 (2013).
79. M. X. Wang, F. Xu, H. F. Sun, Q. Liu, K. Artyushkova, E. A. Stach, and J. Xie, *Electrochim. Acta*, **56**, 2566 (2011).
80. W. Zhang, M. Dubois, K. Guérin, A. Hamwi, J. Giraudet, and F. Masin, *J. Solid State Chem.*, **181**, 1915 (2008).
81. M. Dubois, K. Guérin, E. Petit, N. Batisse, A. Hamwi, N. Komatsu, J. Giraudet, P. Pirotte, and F. Masin, *J. Phys. Chem. C*, **113**, 10371 (2009).
82. H. S. Oh, J. G. Oh, Y. G. Hong, and H. Kim, *Electrochim. Acta*, **52**, 7278 (2007).
83. F. Gloaguen, F. Andolfatto, R. Durand, and P. Ozil, *J. Appl. Electrochem.*, **24**, 863 (1994).
84. A. Kabbabi, F. Gloaguen, F. Andolfatto, and R. Durand, *J. Electroanal. Chem.*, **373**, 251 (1994).
85. A. Gamez, D. Richard, P. Gallezot, F. Gloaguen, R. Faure, and R. Durand, *Electrochim. Acta*, **41**, 307 (1996).
86. Y. Takasu, N. Ohashi, X. G. Zhang, Y. Murakami, H. Minagawa, S. Sato, and K. Yahikozawa, *Electrochim. Acta*, **41**, 2595 (1996).
87. O. Antoine, Y. Bultel, R. Durand, and P. Ozil, *Electrochim. Acta*, **43**, 3681 (1998).
88. Y. Shao-Horn, W. C. Sheng, S. Chen, P. J. Ferreira, E. F. Holby, and D. Morgan, *Topics Catal.*, **46**, 285 (2007).
89. R. W. Pekala, J. C. Farmer, C. T. Alviso, T. D. Tran, S. T. Mayer, J. M. Miller, and B. Dunn, *J. Non-Cryst. Solids*, **225**, 74 (1998).
90. J. Marie, S. Berthon-Fabry, P. Achard, M. Chatenet, A. Pradourat, and E. Chainet, *J. Non-Cryst. Solids*, **350**, 88 (2004).
91. M. Ouattara-Brigaudet, S. Berthon-Fabry, C. Beauger, M. Chatenet, N. Job, M. Sennour, and P. Achard, *Int. J. Hydrogen Energy*, **37**, 9742 (2012).
92. H.-S. Oh, J.-G. Oh, and H. Kim, *J. Power Sources*, **183**, 600 (2008).
93. C. C. Herrmann, G. G. Perrault, and A. A. Pilla, *Anal. Chem.*, **40**, 1173 (1968).
94. L. Dubau, T. Asset, R. Chattot, C. Bonnaud, V. Vanpeene, J. Nelayah, and F. Maillard, *ACS Catal.*, **5**, 5333 (2015).
95. K. Guérin, J. P. Pinheiro, M. Dubois, Z. Fawal, F. Masin, R. Yazami, and A. Hamwi, *Chem. Mater.*, **16**, 1786 (2004).
96. A. Zana, J. Speder, N. E. A. Reeler, T. Vosch, and M. Arenz, *Electrochim. Acta*, **114**, 455 (2013).
97. L. Dubau, M. Lopez-Haro, L. Castanheira, J. Durst, M. Chatenet, P. Bayle-Guillemaud, L. Guétaz, N. Caqué, E. Rossinot, and F. Maillard, *Appl. Catal. B*, **142–143**, 801 (2013).
98. X. Hao, L. Quach, J. Korah, W. A. Spieker, and J. R. Regalbuto, *J. Mol. Catal. A.*, **219**, 97 (2004).
99. N. Job, S. Lambert, M. Chatenet, C. J. Gommes, F. Maillard, S. Berthon-Fabry, J. R. Regalbuto, and J.-P. Pirard, *Catal. Today*, **150**, 119 (2009).
100. X. Hao, S. Barnes, and J. R. Regalbuto, *J. Catal.*, **279**, 48 (2011).
101. F. Maillard, S. Schreier, M. Hanzlik, E. R. Savinova, S. Weinkauf, and U. Stimming, *Phys. Chem. Chem. Phys.*, **7**, 385 (2005).
102. F. Maillard, E. R. Savinova, and U. Stimming, *J. Electroanal. Chem.*, **599**, 221 (2007).
103. L. Dubau, J. Nelayah, S. Moldovan, O. Ersen, P. Bordet, J. Drnec, T. Asset, R. Chattot, and F. Maillard, *ACS Catal.*, **6**, 4673 (2016).
104. T. Asset, R. Chattot, J. Nelayah, N. Job, L. Dubau, and F. Maillard, *ChemElectroChem*, **3**, 1591 (2016).
105. P. J. Ferreira and Y. Shao-Horn, *Electrochem. Solid-State Lett.*, **10**, B60 (2007).

Downloaded on 2018-05-04 to IP 77.158.181.1 address. Redistribution subject to ECS terms of use (see ecsdl.org/site/terms_use) unless CC License in place (see abstract).

106. A. P. Saab, F. H. Garzon, and T. A. Zawodzinski, *J. Electrochem. Soc.*, **149**, A1541 (2002).
107. J. H. Jang, S. Jeon, J. H. Cho, S. K. Kim, S. Y. Lee, E. Cho, H. J. Kim, J. Han, and T. H. Lim, *J. Electrochem. Soc.*, **156**, B1293 (2009).
108. Z. Siroma, J. Hagiwara, K. Yasuda, M. Inaba, and A. Tasaka, *J. Electroanal. Chem.*, **648**, 92 (2010).
109. J. A. Shetzline and S. E. Creager, *J. Electrochem. Soc.*, **161**, H917 (2014).
110. E. N. Gribov, N. V. Maltseva, V. A. Golovin, and A. G. Okunev, *Int. J. Hydrogen Energy*, **41**, 18207 (2016).
111. C. Galeano, J. C. Meier, V. Peinecke, H. Bongard, I. Katsounaros, A. A. Topalov, A. Lu, K. J. J. Mayrhofer, and F. Schüth, *J. Am. Chem. Soc.*, **134**, 20457 (2012).
112. E. Pizzutilo, J. Knossalla, S. Geiger, J. P. Grote, G. Polymeros, C. Baldizzone, S. Mezzavilla, M. Ledendecker, A. Mingers, S. Cherevko, F. Schüth, and K. J. J. Mayrhofer, *Adv. Energy Mater.*, **7** (2017).
113. J. Xie, D. L. Wood Iii, K. L. More, P. Atanassov, and R. L. Borup, *J. Electrochem. Soc.*, **152**, A1011 (2005).
114. J. Xie, D. L. Wood Iii, D. M. Wayne, T. A. Zawodzinski, P. Atanassov, and R. L. Borup, *J. Electrochem. Soc.*, **152**, A104 (2005).

Downloaded on 2018-05-04 to IP **77.158.181.1** address. Redistribution subject to ECS terms of use (see **ecsdl.org/site/terms_use**) unless CC License in place (see abstract).